

ORIGINAL ARTICLE

Electrochemical half-reaction-assisted sub-bandgap photon sensing in a graphene hybrid photodetector

Ze Xiong^{1,6}, Jiawei Chen^{1,6}, Jizhuang Wang¹, Yu Cai¹, Xiang Liu², Zhicheng Su², Shijie Xu², Arshad Khan³, Wendi Li³, Juncao Bian⁴, Gaomin Li⁵, Mingyuan Huang⁵ and Jinyao Tang¹

The photogating effect has been previously utilized to realize ultra-high photoresponsivity in a semiconductor-graphene hybrid photodetector. However, the spectral response of the graphene hybrid photodetector was limited by the bandgap of the incorporated semiconductor, which partially compromised the broadband absorption of graphene. Here, we show that this limitation can be overcome in principle by harnessing the electron-accepting ability of the electrochemical half-reaction. In our new graphene phototransistor, the electrochemical half-reaction serves as an effective reversible electron reservoir to accept the photoexcited hot electron from graphene, which promotes the sub-bandgap photosensitivity in a silver chloride (AgCl)-graphene photodetector. The photoconductive gain of $\sim 3 \times 10^9$ electrons per photon in the AgCl-graphene hybrid is favored by the long lifetime of photoexcited carriers in the chemically reversible redox couple of AgCl/Ag^0 , enabling a significant visible light (400–600 nm) responsivity that is far beyond the band-edge absorption of AgCl. This work not only presents a new strategy to achieve an electrically tunable sub-bandgap photoresponse in semiconductor-graphene heterostructures but also provides opportunities for utilizing the electrochemical half reaction in other two-dimensional systems and optoelectronic devices. *NPG Asia Materials* (2017) 9, e436; doi:10.1038/am.2017.179; published online 6 October 2017

INTRODUCTION

Ultrathin two-dimensional (2D) nanomaterials are a new class of materials that have exotic properties for application in next generation electronics and optoelectronic devices. These properties include gate-tunable electronic properties, high transparency, and excellent mechanical flexibility and compatibility with current silicon-based microfabrication processes. Owing to its intriguing electronic and optical properties, graphene has been studied extensively over the past decade as a promising material for broadband photodetectors.^{1–3} However, due to fast carrier recombination, most graphene-based photodetectors suffer from low responsivity ($< 10 \text{ mA W}^{-1}$).

By contrast, graphene hybrid phototransistors^{4–8} provide high photoresponsivity by incorporating a layer of light absorbing material, such as a layer of semiconducting quantum dots (QDs),^{9–13} which is in contact with the graphene. Upon illumination, the photoexcited carriers in the QDs can be injected into graphene while the charged QDs layer can modulate the conductance of graphene by capacitive coupling. Owing to the long lifetime of injected carriers (τ_{lifetime}) in QDs, a high photoconductive gain G ($G = \tau_{\text{lifetime}}/\tau_{\text{transit}}$, where τ_{transit} is the transit time) of $\sim 10^8$ can be achieved.⁹ Since the photon is absorbed by the incorporated light absorbing material, the spectral response of the graphene hybrid phototransistor seems to be fundamentally limited by the bandgap of the integrated materials as

shown in previous studies.^{5–12} However, the internal photoemission from graphene in the graphene-semiconductor hybrid structure provides an alternative method to realizing broadband photo sensing.^{14–16} In this hybrid structure, the photocurrent is generated as the photoexcited hot electron in graphene is injected into the conduction band of the adjacent semiconductor. However, due to the low quantum efficiency and poor light absorption of graphene, only moderate photoresponsivity ($\sim 0.1 \text{ mA W}^{-1}$) was demonstrated,^{14,15} and signal amplification will be required at a later stage for practical application.

In this paper, we report a new graphene-semiconductor hybrid phototransistor in which the internal photoemission signal is locally amplified within the graphene transistor itself. Importantly, we show that the reversible electrochemical redox couple (AgCl/Ag^0) can serve as an efficient electron reservoir to obtain an ultra-high photoconductive gain, which is the key to realizing high photoresponsivity for sub-bandgap photons in graphene hybrid phototransistors. Furthermore, we demonstrated the spectral selectivity in our graphene photodetector by simply tuning the dielectric layer thickness of the substrate, which is favorable for many color-sensitive applications. In our current design, although the spectral response is not as wide as for a PbS-graphene hybrid, in principle, it offers an alternative method to achieve broadband photosensitivity without using strongly light-

¹Department of Chemistry, The University of Hong Kong, Hong Kong, China; ²Department of Physics, The University of Hong Kong, Hong Kong, China; ³Department of Mechanical Engineering, The University of Hong Kong, Hong Kong, China; ⁴Department of Physics and Materials Science, City University of Hong Kong, Hong Kong, China and ⁵Department of Physics, South University of Science and Technology of China, Shenzhen, China

⁶These authors contributed equally to this work.

Correspondence: Dr J Tang, Department of Chemistry, University of Hong Kong, Pokfulam, Hong Kong 999077, China.

E-mail: jinyao@hku.hk

Received 8 May 2017; revised 21 July 2017; accepted 18 August 2017

absorbing narrow-band semiconductor materials, which shows promise for highly transparent photodetectors and other novel optoelectronic devices.

METHODS

Photodetector device fabrication

The process flow of the AgX-graphene hybrid photodetector fabrication is illustrated in Supplementary Figure 1. Monolayer chemical vapor deposition (CVD) graphene on a copper foil (Graphene Laboratories, Inc., Calverton, NY, USA) was spin-coated with poly(methyl methacrylate) (PMMA) and air dried. Then, the copper was removed by etching in 0.1 M $(\text{NH}_4)_2\text{S}_2\text{O}_8$ aqueous solution overnight. The released graphene layer that was attached on the PMMA film was scooped out and rinsed consecutively in several clean DI water baths. Finally, the film was transferred onto various supporting substrates (silicon wafer, a quartz substrate or polyethylene terephthalate (PET) film) and air dried. After dissolving PMMA with a mixture solution of dichloroethane and acetone (1:5, v/v), the graphene was patterned into micro-ribbons with electron beam lithography followed by oxygen plasma etching. Then, 0.5-nm silver was deposited on the lithographically defined central area of the graphene ribbon via thermal evaporation in vacuum at $\sim 1 \times 10^{-6}$ Torr.

Vapor-solid reactions were utilized to convert the Ag nanoparticles into the AgCl nanoparticles. A 5-ml glass vial with the sample substrate was placed in a sealed 25-ml glass vial together with 0.05 g of KClO_3 solid crystals. Then, 0.15 ml of 37% HCl solution was added to the solid KClO_3 , and the Cl_2 was generated via an *in situ* reaction ($\text{KClO}_3 + 6 \text{HCl} = \text{KCl} + 3 \text{Cl}_2 + 3 \text{H}_2\text{O}$) and allowed to react with Ag nanoparticles on the sample substrate for 10 min at room temperature. For the AgBr nanoparticle synthesis, a 5-ml glass vial with the sample substrate was placed in a sealed 25-ml glass vial with 0.05 g of solid KBr. Then, 0.15 g of solid KMnO_4 and 98% H_2SO_4 solution were added to the solid, and Br_2 vapor was produced via reaction ($2 \text{KMnO}_4 + 8 \text{H}_2\text{SO}_4 + 10 \text{KBr} = 6 \text{K}_2\text{SO}_4 + 5 \text{Br}_2 + 2 \text{MnSO}_4 + 8 \text{H}_2\text{O}$) and allowed to react with Ag nanoparticles for 10 min at room temperature. For the AgI nanoparticle synthesis, the sample substrate was placed in a sealed 25-ml glass vial containing 0.05 g of solid I_2 . Then, the reaction vial was heated to 105 °C to allow the I_2 vapor to react with Ag nanoparticles for 10 min. After the vapor-solid conversion, 5-nm Al_2O_3 was coated using atomic layer deposition (Cambridge NanoTech, Inc., Waltham, MA, USA, Savannah 200) using trimethylaluminum (Sigma-Aldrich, Inc., St Louis, MO, USA) as the precursor at 70 °C. The Al_2O_3 on the electrical contact area was removed by dipping in a 5:1 buffered HF solution for ~ 1 s. The electrodes were patterned on the graphene ribbon using electron beam lithography, followed by 100-nm nickel (Ni) sputtering.

Transmission electron microscope (TEM) sample preparation

As shown in Supplementary Figure 3, the monolayer CVD graphene on copper was spin-coated with PMMA and air dried. After copper removal, the graphene film was rinsed in DI water and scooped onto the TEM grid (SPI Supplies, Inc., West Chester, PA, USA, G200HS) with a 5-nm Al_2O_3 coating produced via atomic layer deposition. Then, 0.5-nm Ag was deposited through the mesh of the grid onto graphene via thermal evaporation and individually reacted with Cl_2 , Br_2 and I_2 . After the reaction, another 5 nm of Al_2O_3 was coated over the device via atomic layer deposition at 70 °C to protect the AgX-graphene surface.

KPFM measurement

The device with graphene on top of the AgCl nanoparticles was prepared using a TEM grid-assisted dry transfer method similar to the TEM sample preparation. The monolayer CVD graphene supported with PMMA film was scooped by the Al_2O_3 -coated TEM grid. After the AgCl conversion reaction, PMMA-supported graphene was transferred onto a clean Si substrate with 470 nm of a thermal oxide and baked on the hot plate at 120 °C for 5 min to improve the adhesion between the graphene and the substrate. Then, the PMMA on graphene was removed by rinsing with a mixture solution of dichloroethane and acetone (1:5, v/v), followed by isopropanol rinsing and blow drying with nitrogen. A 15-nm Au electrode was patterned on the graphene surface as a work function reference via electron beam lithography and thermal evaporation. The KPFM measurement was performed using an Asylum Research MFP-3D-SA atomic force microscope under ambient

conditions. Asylum Research ASYELEC-01 cantilevers with titanium and iridium coatings (3 nm/17 nm) were used at a resonance frequency of 72.394 kHz with a tip voltage of +3.0 V with respect to the ground. The illumination during scanning was achieved by utilizing a Fiber-Liter MI-150R illuminator with a remote controller (Dolan-Jenner Industries, Boxborough, MA, USA).

Photoresponse measurements

The temporal photoresponse and gate tunability of the AgX-G hybrid device were measured using a white light LED light source with an adjustable power output. The spectral response of the hybrid photodetector was measured using an SVX 1450 xenon lamp light source (Müller Elektronik-Optik, Moosinning, Germany) and an Acton SP 300i monochromator equipped with 1200 lines per mm of grating. The photocurrents of the samples were measured using a Keithley 2400 Source Meter. The eQE was measured with a super continuum laser (YSL Photonics, Wuhan, Hubei, China, Supercontinuum Source SC-PRO) with a laser pulse of ~ 100 ps and a repetition rate of 3 MHz. The photoresponsivities at 400 and 500 nm were measured using a monochromatic LED to provide uniform illumination. All light source intensities were calibrated using a standard silicon diode (Hamamatsu S1336-BQ) and an optical power meter (Molelectron Detector, Inc. Portland, OR, USA, POWER MAX 500D).

Finite-difference-time-domain simulation

The power absorption spectrum of the AgCl-graphene heterostructure was calculated using a finite-difference-time-domain software package (Lumerical Solutions, Inc., Vancouver, BC, Canada, FDTD Solutions). Since the nanoparticles were well dispersed, a single AgCl sphere with a diameter of 18 nm on monolayer graphene was modeled, which showed no significant difference from the model with multiple AgCl spheres. A 5-nm Al_2O_3 capping layer was also included in the model. The optical constants of Al_2O_3 , SiO_2 and Si were selected from the software database (Palik, E.D., Handbook of Optical Constants). The absorption simulation was performed with a cross-section analysis module, total-field scattered-field light source and perfectly matched layers boundary conditions without light polarization.

RESULTS

Photodetector design, device fabrication and temporal photoresponse

We fabricated the phototransistors using a silver halide-graphene hybrid (AgX-G, X = Cl, Br, I) as depicted in the schematic diagram (Figure 1a). Degenerately p-doped Si substrate with 470-nm thermal oxide was used as the back-gate electrode to modulate the Fermi level of the AgX-G hybrid. Well-dispersed silver nanoparticles were deposited on the CVD graphene via thermal evaporation (see Methods and Supplementary Figure 1). Then, the Ag nanoparticles were completely converted into AgX nanoparticles by allowing the Ag nanoparticles to react with the respective halogen gas ($2\text{Ag}_{(s)} + \text{X}_{2(g)} \rightarrow 2\text{AgX}_{(s)}$) as observed in X-ray photoelectron spectroscopy (Supplementary Figure 2). After the reaction, the AgX nanoparticles were well dispersed on the graphene surface (Supplementary Figures 3 and 4) with an average diameter of 18 nm. Finally, 5-nm Al_2O_3 was coated over the device surface with atomic layer deposition to minimize the influence of ambient gas molecule adsorption and desorption upon illumination. To estimate the possible contribution of the plasmonic absorption from the trace amount of unreacted Ag metal on the graphene surface, a control device was fabricated with silver nanoparticles over the graphene surface. Because no detectable photoresponse was observed in this control sample (Supplementary Figure 5), it was safe to conclude that the Ag metal plasmonic contribution to the photoresponse in our device was insignificant.

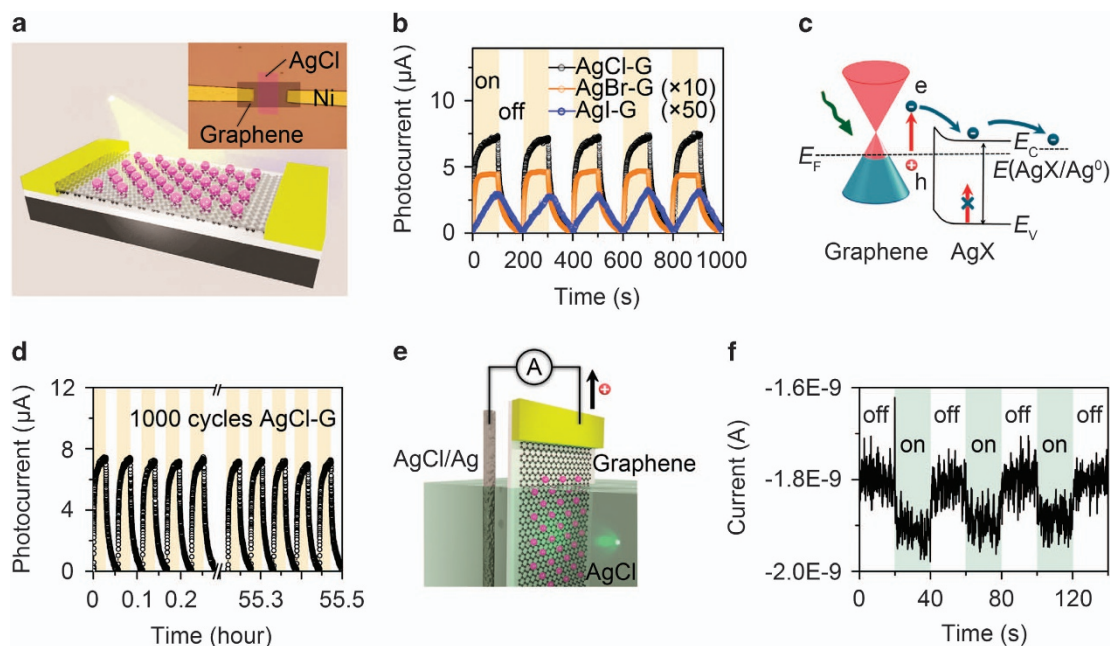


Figure 1 AgCl-graphene photodetector and temporal photoresponse. (a) A schematic diagram of the silver halide-graphene (AgX-G, X=Cl, Br, I) photodetector. Inset: A false colored optical image of the as-prepared AgCl-G photodetector. (b) The temporal photoresponse of the as-prepared AgX-G hybrid photodetectors. The visible light illumination power is ~ 54.9 nW, and the source-drain voltage (V_{SD}) is 1 V. The photocurrents of AgBr-G and AgI-G have been magnified by 10 and 50 times, respectively, for clarity. (c) The energy band diagram at the junction formed by graphene and the semiconducting AgX. For low-energy photons, the AgX cannot be excited directly due to its wide bandgap ($E_g^{AgCl} = 3.25$ eV, $E_g^{AgBr} = 2.69$ eV, $E_g^{AgI} = 2.83$ eV).²⁸ Instead, the hot electrons generated in graphene are injected into the conduction band of the AgX nanoparticles through internal photoemission and transferred to the redox level of AgX/Ag^0 . (d) The long-time (1000 cycles) temporal photoresponse of the AgCl-G photodetector after 6 months of preservation under ambient conditions. (e) The schematic diagram of the photoelectrochemical measurement setup for internal photoemission at the AgCl-graphene junction. (f) The temporal photoelectrochemical response of the AgCl-G working electrode at a 0-V bias under chopped green light illumination (520 nm wavelength).

We examined the photoresponse of hybrid phototransistors with AgCl, AgBr or AgI under the same visible illumination. Since AgCl is a wide bandgap ($E_g^{AgCl} = 3.25$ eV) semiconductor, only ultraviolet sensitivity is expected (Supplementary Figure 6), assuming the same sensing mechanism as previously reported for a graphene-semiconductor hybrid phototransistor.^{9–13} By contrast, a high photoresponse was observed with visible light illumination, suggesting a new sensing mechanism in our phototransistor. Figure 1b shows the photocurrent (after dark current subtraction) of the as-prepared AgX-G photodetectors at room temperature under chopped light illumination (white light illumination with a power of ~ 54.9 nW) at a 1-V source-drain voltage (V_{SD}) and a 0-V back-gate voltage (V_G). If working as a traditional graphene hybrid phototransistor in which the semiconductor is responsible for light absorption, the photoresponse of the AgI-G hybrid should be the highest because AgI has the lowest bandgap and the highest photosensitivity. However, the observed photoresponse of the AgCl-G hybrid is much stronger than that of AgBr-G and AgI-G, which strongly suggests that the photoresponse did not originate from AgX nanoparticle absorption. To explain this phenomenon, we attributed this sub-bandgap photosensitivity in our device to the electrochemically assisted internal photoemission from graphene to the AgX nanoparticles. As illustrated in Figure 1c, upon illumination with low-energy photons, the photoexcited hot carriers with an energy higher than the Schottky barrier height (Φ_B) can be injected into the AgX nanoparticles¹⁷ and then stored into the low-energy redox level of AgX/Ag^0 by inducing the half electrochemical reduction reaction $AgX + e^- \rightarrow Ag^0 + X^-$, which will negatively charge the AgX nanoparticles and enhance the conductance of the graphene transistor via capacitive coupling. In the dark, the reduction

reaction is reversed and the injected electron is released back to graphene through a tunneling process, restoring the phototransistor back to its low conductance state. Here, the sub-bandgap photoresponsivity of the graphene hybrid detector is primarily determined by the nanoparticle's ability to accept electrons. In electrochemistry, the electrochemical potential (E) is classically used to represent the ability of an oxidant to accept electrons. In our case, since AgCl is a stronger oxidant than AgBr and AgI ($E_{AgCl/Ag} = -4.66$ eV $< E_{AgBr/Ag} = -4.51$ eV $< E_{AgI/Ag} = -4.29$ eV)¹⁸ and readily retains the injected hot carriers from the graphene, the highest gain and photoresponsivity were observed in AgCl-G, followed by AgBr-G and AgI-G. This result suggested that the classical standard electrochemical potential could also be used to benchmark the electron-accepting ability of other electrochemical reaction-assisted graphene hybrid phototransistors for low energy photon sensing. Without a favorable redox couple (for example, in the ZnO-graphene hybrid), the internal photoemission from graphene to the semiconductor is insignificant and the sub-bandgap photoresponse is negligible.^{10,11} Since our phototransistor involves an electrochemical redox reaction, it is important to assess the stability of our device, which is determined by the reversibility of the redox reaction. The AgCl-G sample was stored under ambient conditions for 6 months and then subjected to a long stress test under chopped illumination (Figure 1d). After over 1000 on–off cycles, the photocurrent maintained the same level, indicating the great reversibility and reliability of our device.

To confirm the sensing mechanism in our phototransistor, we prepared a photoelectrochemical electrode based on the AgCl-G hybrid to test the internal photoemission current from graphene to the AgCl nanoparticles at a 0-V bias. As shown in Figure 1e, AgCl

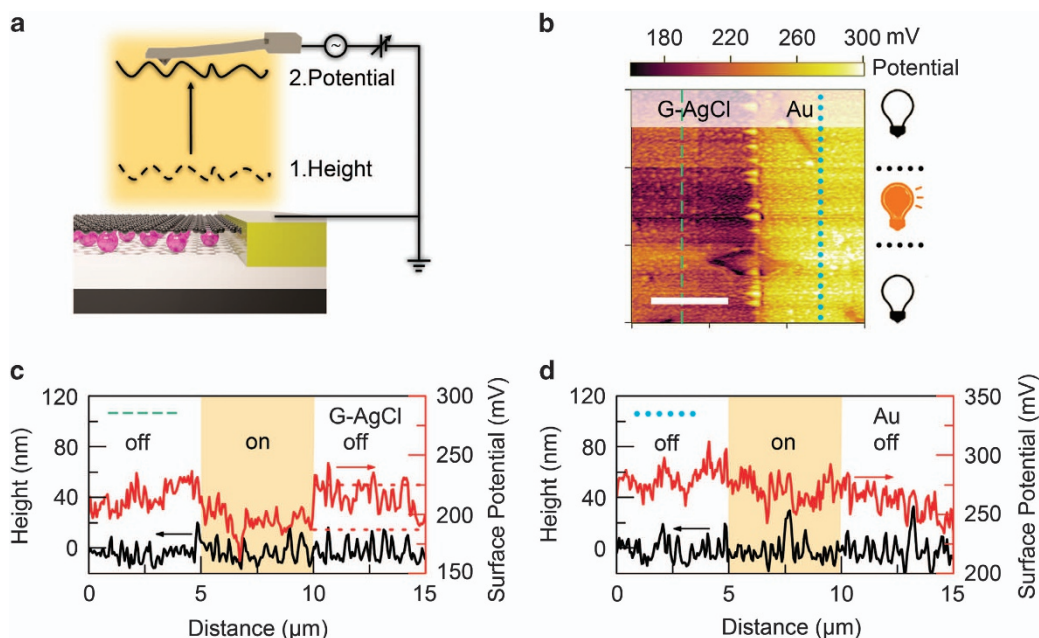


Figure 2 Structure and surface potential profiles of graphene-AgCl. (a) KPFM setup for the two-pass technique. (b) KPFM image taken on the surface of graphene-AgCl (left) and the Au electrode (right) under alternating ‘dark’, ‘light’ and ‘dark’ illumination states at $V_G = 0$ V. Scale bar: 5 μm . (c) Height and surface potential profiles along the green dashed lines on the graphene-AgCl surface. (d) Height and surface potential profiles along the blue dotted lines on the Au surface. KPFM, Kelvin probe force microscopy.

nanoparticle-loaded monolayer graphene was used as a working electrode and submerged into a 1 M KCl solution with AgCl/Ag as the counter electrode. Upon illumination with low-energy photons (520 nm), the AgCl could not be excited while the hot electron was generated in graphene. We recorded the temporal photocurrent at the 0-V bias in chopped green light illumination, as shown in Figure 1f. Since no detectable photocurrent was observed for AgCl nanoparticles over the platinum surface (Supplementary Figure 7), which has a similar work function as graphene ($\Phi_{\text{graphene}} = 4.95.1$, $\Phi_{\text{Pt}} = 5.1$),¹⁹ the photocurrent clearly did not originate from the AgCl absorption and should be attributed to the graphene internal photoemission similar to the recently demonstrated graphene-semiconductor photodetector.^{14,15} In this mechanism, since the internal photoemission is controlled by the Schottky barrier height at the graphene-semiconductor interface instead of the bandgap of the incorporated semiconductor, our photodetector is capable of exploiting sub-bandgap photons and extending the sensitivity to the visible spectrum. This strategy offers a new approach to engineer the spectral response of optoelectronic devices via surface engineering without using narrow bandgap materials.

KPFM characterization

To further verify the internal photoemission process at the AgCl-graphene junction, Kelvin probe force microscopy (KPFM) was utilized to investigate the surface potential modulation of graphene under different illumination conditions (Supplementary Figure 8). Because the KPFM measurement is highly surface-sensitive, a sample with graphene on top of AgCl (G-AgCl) was prepared (see Methods). As shown in Figures 2a and b, the surface potential image was taken using the standard two-pass technique while the electrically grounded Au electrode was used as an internal reference to show the surface potential change upon illumination.

The surface potential in the KPFM measurement is determined by the contact potential difference between the probe and the

sample surface. Given the identical probe conditions, the difference in the work function between the Au electrode (Φ_{Au}) and the G-AgCl (Φ_g) can be related to the surface potential difference, ΔV_{CPD} , as $e\Delta V_{\text{CPD}} = e(V_g - V_{\text{Au}}) = \Phi_{\text{Au}} - \Phi_g$,²⁰ where V_{Au} and V_g are the average surface potential of the Au electrode and the G-AgCl, respectively. Hence, the work function of graphene can be quantified after taking the work function of the electrically grounded Au electrode ($\Phi_{\text{Au}} = 4.82$ eV).²¹ The surface potential profiles in Figures 2c and d show that the work function of G-AgCl upshifts from a ‘dark state’ ($\Phi_g^{\text{dark}} \approx 4.88$ eV) to a ‘light state’ ($\Phi_g^{\text{light}} \approx 4.90$ eV), whereas no detectable shift in work function was observed on the Au electrode. Additionally, there was no distinguishable potential change after visible light illumination in the control sample made of graphene without AgCl nanoparticles (Supplementary Figure 9c), which indicates that the photoexcited hot electrons were emitted from graphene to the AgCl nanoparticles upon illumination. The photoactive area in our AgCl-G device is not constrained to the vicinity of the Au electrode, which allows a larger photoactive area for photon harvesting than that of photovoltaic graphene photodetectors.^{1,2}

Sub-bandgap photoresponse of the AgCl-graphene hybrid

The performance of the AgCl-G phototransistor under visible illumination was further explored in detail. Figure 3a shows the dependence of responsivity on V_{SD} under 500-nm illumination with different powers at $V_G = 0$ V (400 nm illumination, see Supplementary Figure 10). The raised responsivity at higher V_{SD} values can be ascribed to the shortened transit time and the subsequently improved gain value. Figure 3b plots the responsivity as a function of the light power for 500-nm illumination at $V_{\text{SD}} = 1$ V and $V_G = 0$ V. A high responsivity of $\sim 7.3 \times 10^4$ AW^{-1} was obtained under an illumination power of 16.4 pW. Under a higher illumination intensity, the photoresponsivity gradually decreases because the filling of the AgCl/Ag⁰ reservoir prevents the accepting of additional photocarriers and shortens the average τ_{lifetime} .¹⁰

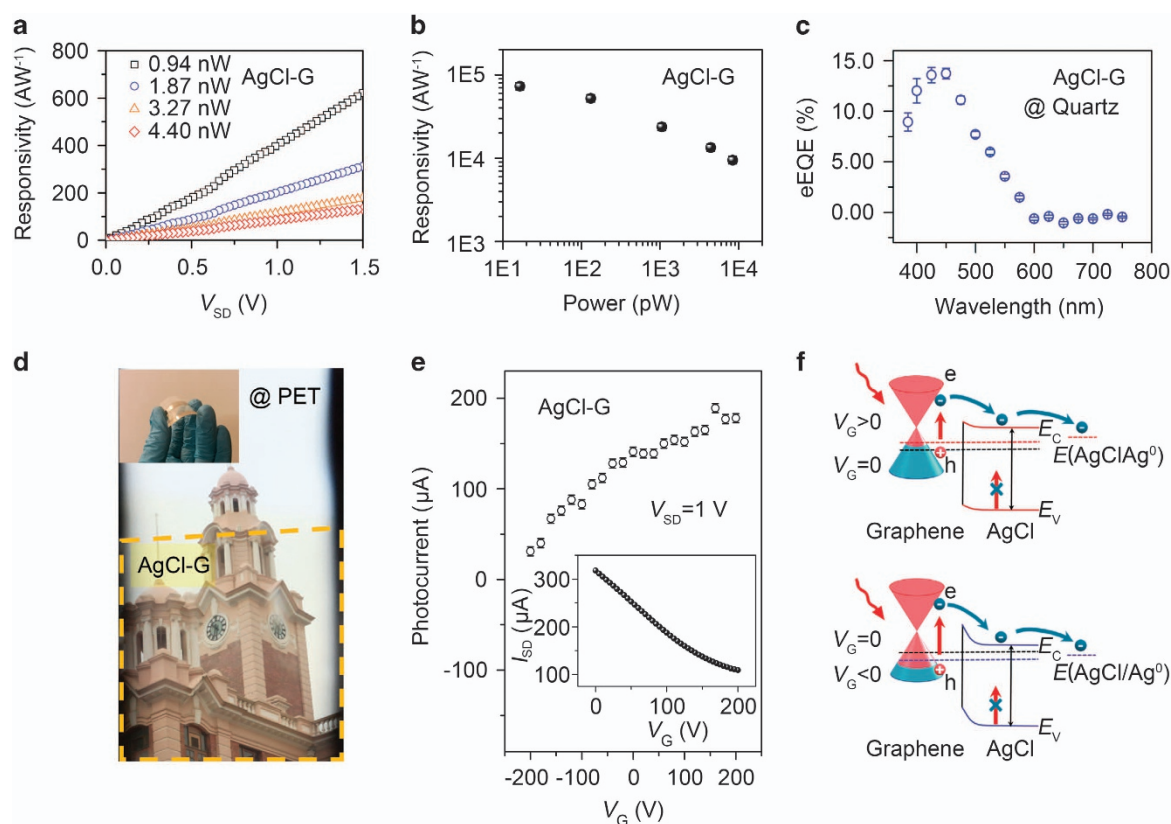


Figure 3 Sub-bandgap and gate-tunable photoresponse. (a) The photoresponsivity increases linearly with V_{SD} under 500-nm illumination of different optical input powers at $V_G = 0$ V. (b) Photoresponsivity as a function of the optical input power under 500-nm illumination at $V_{SD} = 1$ V and $V_G = 0$ V. (c) The effective external quantum efficiency (eEQE) of the AgCl-G sample on quartz at $V_{SD} = 1$ V. (d) A photo of the University's main building taken through flexible AgCl-G (the area of AgCl-G is highlighted by a brown dashed line) on PET film. Inset: A photographic image of the flexible AgCl-G photodetector on PET film. (e) The photocurrent of AgCl-G as a function of V_G under 500-nm light illumination with a power of ~ 5.42 nW at $V_{SD} = 1$ V. Inset: Transfer characteristics of the AgCl-G phototransistor in the dark state, showing p-type doping in graphene by AgCl nanoparticles. (f) Energy band diagram of the AgCl-G phototransistor at different V_G values. The dashed lines correspond to the Fermi level of graphene at various V_G (black for $V_G = 0$, red for $V_G > 0$ and blue for $V_G < 0$) values.

To evaluate the intrinsic spectral response of AgCl-G, the effective external quantum efficiency (eEQE) was estimated by multiplying the external quantum efficiency by the photoconductivity gain of the device (Figure 3c).⁵ A AgCl-G sample on a quartz substrate was measured with monochromatic illumination. The eEQE had a pronounced value in the visible range from 385 to 600 nm (13.6% at 425 nm) beyond the band edge of AgCl. As predicted by the Fowler theory,²² hot carriers with lower energy have less photoemission probability, which leads to the decreasing of eEQE towards a longer wavelength. When the light wavelength goes below 425 nm, the photoexcited electrons from AgCl itself will partially occupy the AgCl/Ag⁰ redox couple, hindering the collection of photocarriers from graphene and lowering the eEQE. Owing to the low light absorbance of the graphene and the ultrathin AgCl layer, a transparent AgCl-G phototransistor with a high transmittance of $\sim 92.8\%$ could be prepared on PET film (Figure 3d).

The carrier mobility (μ) of the graphene channel in AgCl-G without illumination was calculated to be $362.2 \text{ cm}^2 \text{ V}^{-1} \text{ s}^{-1}$ from the transfer characteristic measurement (Figure 3e, inset) using $\mu = (dI_{SD}/dV_G) \times [L/(WC_i V_{SD})]$, where L is the channel length (22 μm), W is the channel width (16 μm) and C_i is the areal capacitance (7.34 nF cm⁻², SiO₂ thickness of 470 nm).²³ The gate tunability of the photocurrent in the AgCl-G device is shown in Figure 3e under a uniform 500-nm light illumination with a power of ~ 5.42 nW at $V_{SD} = 1.0$ V (385 nm light illumination see

Supplementary Figure 11). As shown in Figure 3f, a negative V_G leads to a lower Fermi level in graphene and a raised barrier height at the AgCl-graphene junction, which mitigates the hot electron injection into AgCl and leads to lower overall photoresponsivity.

Spectral selectivity modulation

The spectral selectivity in graphene has previously been realized by integrating with various photonic devices via sophisticated fabrication processes.^{24–26} We demonstrate that, in our phototransistor, the spectral selectivity can be accomplished by simply modulating the thickness of the thermal oxide underneath the graphene layer (Figure 4a). As shown in Figure 4b, for AgCl-G on a silicon substrate with 470 nm of SiO₂, two major responsivity peaks at 400 and 500 nm were observed. This enhancement can be attributed to the optical resonance inside the dielectric layer, which resembled the spectral response of single-layer graphene on 300-nm SiO₂.³ The power absorption spectrum predicted by the finite-difference-time-domain simulation matches well with the experimental data. As a comparison, only a single photoresponse peak located at approximately 400 nm could be identified for a photodetector fabricated on a 200-nm SiO₂ substrate as calculated by the finite-difference-time-domain simulation. An overview of the spectral selectivity upon changing the oxide thickness is shown in Figure 4c.

In contrast to the previously demonstrated graphene-semiconductor phototransistor, our phototransistor relies on the photon absorption

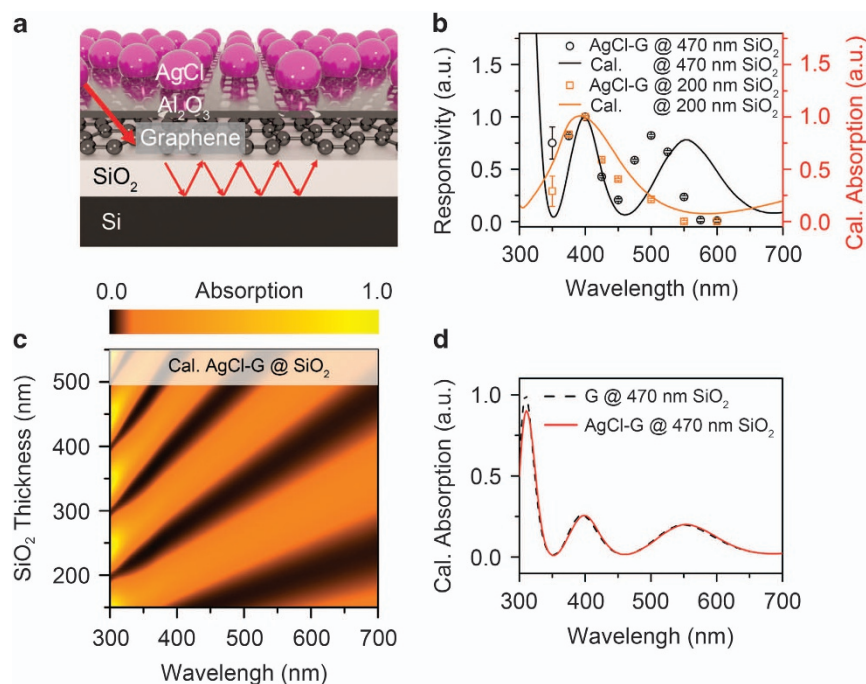


Figure 4 Spectral selectivity modulation. (a) Illustration of multiple reflections within the dielectric layer beneath the monolayer graphene. (b) The experimental wavelength-dependent responsivity of AgCl-G on thermal oxide substrates at $V_{SD}=1$ V and $V_G=0$ V (black circles for 470-nm SiO_2 and brown squares for 200-nm SiO_2 , left axis) and corresponding FDTD-calculated absorption spectra (black line for 470-nm SiO_2 and brown line for 200-nm SiO_2 , right axis). All of the data were normalized to the responsivity at 400 nm. (c) Absorption intensity map for AgCl-G as a function of both the excitation wavelength and the SiO_2 thickness. (d) The calculated absorption of AgCl-G and bare graphene on 470-nm SiO_2 after normalization to the peak value of bare graphene. FDTD, finite-difference-time-domain.

in the graphene layer rather than in the semiconductor. As shown in Figure 4d, the simulated absorption spectra of AgCl-G and bare graphene match well with each other in the visible region, indicating that the light absorption in AgCl is negligible for the AgCl-G heterostructure. The power absorption ratio between graphene (P_{graphene}) and AgCl (P_{AgCl}) is 126:1 for 400-nm incident wavelength and even higher for 500 nm (246:1) (Supplementary Figure 12), which again confirms the distinct sensing mechanism of the AgCl-G hybrid phototransistor.

DISCUSSION

Photoconductive gain is a key figure of merit for a photodetector. Based on the mobility value in AgCl-G, the transit time ($\tau_{\text{transit}} = L^2 \mu^{-1} V_{SD}^{-1}$) of the carriers is ~ 2.76 ns.¹⁰ Therefore, the photoconductive gain is estimated to be $\sim 3.04 \times 10^9$ by adopting $\tau_{\text{lifetime}} = 8.4$ s (Figure 1b, $\sim 50\%$ photocurrent decay), which is over 30 times larger than the value of a PbS QD-graphene hybrid photodetector.⁹ Because the photoconductive gain scales linearly with the mobility of graphene, we can expect that the responsivity can be further improved by adopting boron nitride²⁷ or a self-assembled monolayer-coated oxide¹⁰ as the substrate. One drawback of our device is that the response speed is slower compared to the previously demonstrated graphene hybrid photodetector primarily due to its slow turnoff speed. This is understandable because the AgCl nanoparticles in our device are *in situ* synthesized by gas phase halogenation in which more deep trap states are present on the AgCl surface compared to solution-synthesized QDs, which significantly slows down the charge released in the dark. To facilitate the charge releasing, we applied a positive reset pulse at the gate electrode, which lowered the Fermi level of graphene and promoted the charge extraction from the trap states in AgCl to graphene.⁹ As shown

in Supplementary Figure 13, the transit time of our photodetector can be effectively reduced to 2.3 s by introducing the reset pulse. We expect that by improving the synthesis process and introducing surface passivation to the AgCl, a further improved response speed can be achieved. Moreover, ZnO has a band structure that is similar to AgCl (bandgap $E_g^{\text{ZnO}} = 3.2$ eV, $E_g^{\text{AgCl}} = 3.25$ eV; conduction band minimum $E_c^{\text{ZnO}} = -4.19$ eV, $E_c^{\text{AgCl}} = -4.3$ eV and valence band maximum $E_v^{\text{ZnO}} = -7.39$ eV, $E_v^{\text{AgCl}} = -7.55$ eV);^{28–31} however, only an ultraviolet response was observed in a ZnO-graphene hybrid.^{8,10,11} This fact indicated the vital role of the AgCl/Ag⁰ redox couple in our photodetector. To evaluate the noise characteristics of our photodetector, the noise-equivalent-power, which is the optical power that yields a unity signal-to-noise ratio for a given bandwidth, was estimated by analyzing the noise in the dark current (Supplementary Figure 14).³² A noise-equivalent-power of $\sim 10^{-14}$ W Hz^{-1/2} can be achieved at a frequency of 1 Hz by dividing the noise spectral density by the responsivity ($\sim 7.3 \times 10^4$ AW⁻¹ at 500 nm, Figure 3b).

In summary, we demonstrated a hybrid graphene phototransistor for sub-bandgap photon sensing by utilizing the electrochemical redox half-reaction of silver chloride as a reversible carrier reservoir. Specifically, an ultrahigh photoconductive gain and photoresponsivity far beyond the absorption band edge of AgCl was achieved. Our experiment and simulation results reveal that graphene can serve as a light absorbing material in a hybrid graphene phototransistor in which the spectral response is no longer limited by the integrated semiconducting material. This study not only presents a new paradigm of sub-bandgap absorption in semiconductor-graphene heterostructures but also inspires the broader application of the electrochemical redox half-reaction in other optoelectronic devices.

CONFLICT OF INTEREST

ZX, JC and JT have filed a US patent based on this work (application no. 62/346,706). The remaining authors declare no conflict of interest.

ACKNOWLEDGEMENTS

This work was supported in part by the Hong Kong Research Grants Council (RGC) General Research Fund (GRF17303015, GRF17305917, ECS27300814), the University Grant Council (Contract No. AoE/ P-04/08), the URC Strategic Research Theme on Clean Energy (University of Hong Kong), and the URC Strategic Research Theme on New Materials (University of Hong Kong).

Author contributions: ZX, JC and JT conceived the project. ZX, JC, JW and YC performed the sample preparation and device fabrication. ZX, JC, ZS and SX performed the photocurrent measurements. ZX, XL and AK performed the KPFM measurements. ZX and WL performed the FDTD simulation. JB performed the XPS measurements. GL and MH performed the absorbance measurements. ZX and JT co-wrote the paper with all authors contributing to the discussion and preparation of the manuscript.

PUBLISHER'S NOTE

Springer Nature remains neutral with regard to jurisdictional claims in published maps and institutional affiliations.

- 1 Lemme, M. C., Koppens, F. H. L., Falk, A. L., Rudner, M. S., Park, H., Levitov, L. S. & Marcus, C. M. Gate-activated photoresponse in a graphene p-n junction. *Nano Lett.* **11**, 4134–4137 (2011).
- 2 Mueller, T., Xia, F. & Avouris, P. Graphene photodetectors for high-speed optical communications. *Nat. Photon.* **4**, 297–301 (2010).
- 3 Tielrooij, K. J., Piatkowski, L., Massicotte, M., Woessner, A., Ma, Q., Lee, Y., Myhro, K. S., Lau, C. N., Jarillo Herrero, P., van Hulst, N. F. & Koppens, F. H. L. Generation of photovoltage in graphene on a femtosecond timescale through efficient carrier heating. *Nat. Nanotechnol.* **10**, 437–443 (2015).
- 4 Liu, Y., Wang, F., Wang, X., Wang, X., Flahaut, E., Liu, X., Li, Y., Wang, X., Xu, Y., Shi, Y. & Zhang, R. Planar carbon nanotube-graphene hybrid films for high-performance broadband photodetectors. *Nat. Commun.* **6**, 9589 (2015).
- 5 Lee, Y., Kwon, J., Hwang, E., Ra, C.-H., Yoo, W. J., Ahn, J.-H., Park, J. H. & Cho, J. H. High-performance perovskite-graphene hybrid photodetector. *Adv. Mater.* **27**, 41–46 (2015).
- 6 Wang, Y., Zhang, Y., Lu, Y., Xu, W., Mu, H., Chen, C., Qiao, H., Song, J., Li, S., Sun, B., Cheng, Y.-B. & Bao, Q. Hybrid graphene-perovskite phototransistors with ultrahigh responsivity and gain. *Adv. Opt. Mater.* **3**, 1389–1396 (2015).
- 7 Chen, S.-Y., Lu, Y.-Y., Shih, F.-Y., Ho, P.-H., Chen, Y.-F., Chen, C.-W., Chen, Y.-T. & Wang, W.-H. Biologically inspired graphene-chlorophyll phototransistors with high gain. *Carbon* **63**, 23–29 (2013).
- 8 Chang, H., Sun, Z., Ho, K. Y.-F., Tao, X., Yan, F., Kwok, W.-M. & Zheng, Z. A highly sensitive ultraviolet sensor based on a facile in situ solution-grown ZnO nanorod/graphene heterostructure. *Nanoscale* **3**, 258–264 (2011).
- 9 Konstantatos, G., Badioli, M., Gaudreau, L., Osmond, J., Bernechea, M., de Arquer, F. P. G., Gatti, F. & Koppens, F. H. L. Hybrid graphene-quantum dot phototransistors with ultrahigh gain. *Nat. Nanotechnol.* **7**, 363–368 (2012).
- 10 Shao, D., Gao, J., Chow, P., Sun, H., Xin, G., Sharma, P., Lian, J., Koratkar, N. A. & Sawyer, S. Organic-inorganic heterointerfaces for ultrasensitive detection of ultraviolet light. *Nano Lett.* **15**, 3787–3792 (2015).
- 11 Guo, W., Xu, S., Wu, Z., Wang, N., Loy, M. M. T. & Du, S. Oxygen-Assisted Charge Transfer Between ZnO quantum dots and graphene. *Small* **9**, 3031–3036 (2013).
- 12 Shin, D. H., Kim, S., Kim, J. M., Jang, C. W., Kim, J. H., Lee, K. W., Kim, J., Oh, S. D., Lee, D. H., Kang, S. S., Kim, C. O., Choi, S.-H. & Kim, K. J. Graphene/Si-quantum-dot heterojunction diodes showing high photosensitivity compatible with quantum confinement effect. *Adv. Mater.* **27**, 2614–2620 (2015).

- 13 Zhang, D. Y., Gan, L., Cao, Y., Wang, Q., Qi, L. M. & Guo, X. F. Understanding charge transfer at PbS-decorated graphene surfaces toward a tunable photosensor. *Adv. Mater.* **24**, 2715–2720 (2012).
- 14 Massicotte, M., Schmidt, P., Vialla, F., Watanabe, K., Taniguchi, T., Tielrooij, K. J. & Koppens, F. H. L. Photo-thermionic effect in vertical graphene heterostructures. *Nat. Commun.* **7**, 12174 (2016).
- 15 Wang, X. M., Cheng, Z. Z., Xu, K., Tsang, H. K. & Xu, J. B. High-responsivity graphene/silicon-heterostructure waveguide photodetectors. *Nat. Photon.* **7**, 888–891 (2013).
- 16 Rodriguez-Nieva, J. F., Dresselhaus, M. S. & Song, J. C. W. Enhanced thermionic-dominated photoresponse in graphene Schottky junctions. *Nano Lett.* **16**, 6036–6041 (2016).
- 17 Zheng, B. Y., Zhao, H., Manjavacas, A., McClain, M., Nordlander, P. & Halas, N. J. Distinguishing between plasmon-induced and photoexcited carriers in a device geometry. *Nat. Commun.* **6**, 7797 (2015).
- 18 Vanýsek, P. *CRC Handbook of Chemistry and Physics*, 96th edn (CRC Press, 2015).
- 19 Song, S. M., Park, J. K., Sul, O. J. & Cho, B. J. Determination of work function of graphene under a metal electrode and its role in contact resistance. *Nano Lett.* **12**, 3887–3892 (2012).
- 20 Yu, Y.-J., Zhao, Y., Ryu, S., Brus, L. E., Kim, K. S. & Kim, P. Tuning the graphene work function by electric field effect. *Nano Lett.* **9**, 3430–3434 (2009).
- 21 Panchal, V., Pearce, R., Yakimova, R., Tzalenchuk, A. & Kazakova, O. Standardization of surface potential measurements of graphene domains. *Sci. Rep.* **3**, 2597 (2013).
- 22 Knight, M. W., Sobhani, H., Nordlander, P. & Halas, N. J. Photodetection with active optical antennas. *Science* **332**, 702–704 (2011).
- 23 Schwierz, F. Graphene transistors. *Nat. Nanotechnol.* **5**, 487–496 (2010).
- 24 Engel, M., Steiner, M., Lombardo, A., Ferrari, A. C., Löhneysen, H.-v., Avouris, P. & Krupke, R. Light-matter interaction in a microcavity-controlled graphene transistor. *Nat. Commun.* **3**, 906 (2012).
- 25 Gan, X. T., Shiue, R. J., Gao, Y. D., Meric, I., Heinz, T. F., Shepard, K., Hone, J., Assefa, S. & Englund, D. Chip-integrated ultrafast graphene photodetector with high responsivity. *Nat. Photon.* **7**, 883–887 (2013).
- 26 Echtermeyer, T. J., Britnell, L., Jasnós, P. K., Lombardo, A., Gorbachev, R. V., Grigorenko, A. N., Geim, A. K., Ferrari, A. C. & Novoselov, K. S. Strong plasmonic enhancement of photovoltage in graphene. *Nat. Commun.* **2**, 458 (2011).
- 27 Gannett, W., Regan, W., Watanabe, K., Taniguchi, T., Crommie, M. F. & Zettl, A. Boron nitride substrates for high mobility chemical vapor deposited graphene. *Appl. Phys. Lett.* **98**, 242105 (2011).
- 28 Bose, D. N. & Govindacharyulu, P. A. Physics of silver halides and their applications. *Bull. Mater. Sci.* **2**, 221–231 (1980).
- 29 El Halouani, F. & Deschanvres, A. Interfaces semi-conducteur-electrolyte: correlations entre le potentiel de bande plate et les échelles d'électronégativité. *Mater. Res. Bull.* **17**, 1045–1052 (1982).
- 30 Sumi, S., Watanabe, T., Fujishima, A. & Honda, K. Effect of Cl- and Br- ions and pH on the flatband potentials of silver halide sheet crystal electrodes. *Bull. Chem. Soc. Jpn.* **53**, 2742–2747 (1980).
- 31 Bauer, R. S. & Spicer, W. E. Silver-halide valence and conduction states: temperature-dependent ultraviolet-photoemission studies. *Phys. Rev. B* **14**, 4539–4550 (1976).
- 32 Liu, C. H., Chang, Y. C., Norris, T. B. & Zhong, Z. H. Graphene photodetectors with ultra-broadband and high responsivity at room temperature. *Nat. Nanotechnol.* **9**, 273–278 (2014).



This work is licensed under a Creative Commons Attribution 4.0 International License. The images or other third party material in this article are included in the article's Creative Commons license, unless indicated otherwise in the credit line; if the material is not included under the Creative Commons license, users will need to obtain permission from the license holder to reproduce the material. To view a copy of this license, visit <http://creativecommons.org/licenses/by/4.0/>

© The Author(s) 2017

Supplementary Information accompanies the paper on the NPG Asia Materials website (<http://www.nature.com/am>)